

Robust wavefront segment registration based on a parallel approach

NIKOLAUS BERLAKOVICH^{1,*}, MARTIN FUERST¹, ERNST CSENCICS¹, AND GEORG SCHITTER¹

¹Christian Doppler Laboratory for Precision Engineering for Automated In-Line Metrology, Automation and Control Institute (ACIN), TU Wien,
1040 Vienna, Austria

*Corresponding author: berlakovich@acin.tuwien.ac.at

Abstract: This paper presents a robust registration algorithm for wavefront reconstruction from multiple partial measurements. Wavefronts exceeding the dynamic range or size of the Shack-Hartmann sensor (SHS) can be measured as a set of segments. The wavefront is reconstructed by parallel registration of these wavefront segments, enabling the compensation of sensor misalignment as well as of phase differences. For registration, a global mismatch metric is minimized by rigid body transformations and propagation of the wavefront segments. Apart from the description of the algorithm, simulation-based evaluation and comparison to the iterative closest point (ICP) algorithm is performed. It is shown that in the case of a noisy data set, the parallel approach enables reconstruction errors which are a factor 10 smaller than the result obtained with the ICP algorithm.

© 2021 Optical Society of America

1. Introduction

Shack-Hartmann sensors (SHS) are frequently used for evaluation of optical systems. The SHS enables to directly assess the actual entity of interest, i.e. the wavefront, instead of evaluating the geometrical properties of a lens or other optical device. The measurement with this sensor provides several advantages like insensitivity to vibrations, reference free measurement, large dynamic range and compactness [1,2]. Hence, this sensor is suitable for many optical applications and widely used, e.g., in ophthalmology [3], adaptive optics [4,5], optical system alignment [6] and production of optical systems and components [2].

Nevertheless, optics featuring large wavefronts or wavefronts with huge aberrations can be a challenge for the SHS, as the wavefront might exceed the dynamic range and the aperture of the sensor. Additional supporting optics, e.g. null-optics, can transform the wavefront into a measurable wavefront, but cause additional errors in the measurement and might depend on the specific type of aberration [7,8]. In a recently proposed concept, large or strongly aberrated wavefronts are directly measured with the SHS at different positions and alignments, which leads to a set of measurements including the information of the entire wavefront [9–11]. With the sensor position and alignment of each measurement the wavefront can be reconstructed by transforming each measured part of the wavefront, i.e. a wavefront segment into the global frame (FG). However, due to errors like sensor misalignment or phase difference between wavefront segments, a simple transformation into FG entails large reconstruction errors.

To enable an accurate measurement of the wavefront an algorithm that considers these errors is required. In particular, stitching algorithms turned out to be a good choice for this issue. These algorithms utilize the fact that overlapping measurements have the same information in the overlapping region, which enables wavefront segments to get correctly aligned. There are different concepts for registration of SHS measurements developed. In [12,13] least squares method and active alignment is used to register the wavefront segments. Furthermore, in [14] a wavefront reconstruction based on the popular iterative closest point algorithm (ICP) is proposed.

All these algorithms implement sequential registration concepts [15], where the wavefront segments are consecutively added to the registered wavefront by individual registration processes leading to accumulation of registration errors that might limit evaluation of optical devices, especially if the aberrations of the nominal wavefront are small.

The contribution of this paper is a parallel registration algorithm that reduces accumulation of registration errors and which is therefore more robust to noise than the sequential approach. In particular, all wavefront segments are simultaneously rigidly transformed and propagated to compensate for any rigid misalignment and phase difference between the measurements.

Section 2 introduces the algorithm and discusses its properties, while Section 3 presents a simulative analysis of the algorithm and compares its performance with sequential registration based on the ICP algorithm. Section 4 concludes the paper.

2. Algorithm Description

To capture a wavefront beyond the dynamic range or aperture size of the SHS, the sensor can be moved over the wavefront, taking several measurements [9]. With each measurement the part of the wavefront covered by the sensor aperture is measured, where the sensor aperture with a specific position in space is called a subaperture. In the scope of this study a measured wavefront part is called a wavefront segment. A scan trajectory deviating from the wavefront of a specific phase leads to measurements at different phases as illustrated in Fig. 1. Furthermore, errors in the positioning system cause the sensor to deviate from its nominal position (see Fig. 1). Due to these errors, reconstruction of the entire wavefront based on the nominal positioning data leads to wavefront errors. In particular, the segments reflect sensor misalignment and phase at which they are measured and as a result mismatch between overlapping segments is observed.

To compensate for misalignment and phase difference the wavefront segments are rigid body transformed and propagated as illustrated in Fig. 2. A rigid body transformation enables the translation and rotation of the wavefront in all six spatial degrees of freedom by the use of six parameters - three for translation and rotation, respectively - without altering the shape of the wavefront. The segments are transformed until the overlap mismatch is minimized.

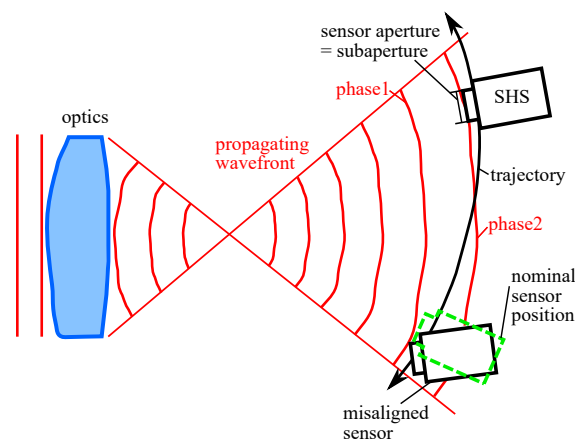


Fig. 1. Wavefront measured at different subapertures. Typically, the sensor is misaligned and the scan trajectory traverses a certain phase interval resulting in measurements of different wavefronts.

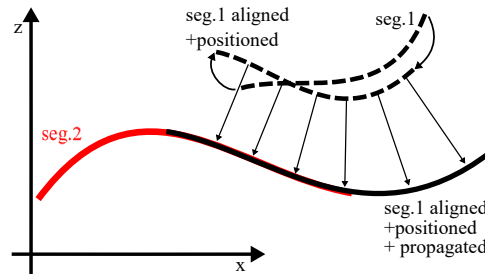


Fig. 2. Mismatch between wavefront segments due to sensor misalignment and phase difference. With suitable alignment and positioning (rigid body transformation) and propagation, the segments can be registered.

2.1. Reconstruction of wavefront segments

A SHS measures the gradients of the incoming wavefront at spots arranged in a grid. There exist several algorithms to reconstruct the wavefront from its gradients, which can be divided into modal and zonal reconstruction. In the modal case the wavefront is described by a series of functions [16], while in the zonal case local assumptions for the wavefront are made [17]. Typically, the latter one better preserves details of the wavefront [18] and, as shape is crucial for an accurate registration result, this type of reconstruction is preferred in this paper. After zonal reconstruction the wavefront shape is in the form of a point cloud, i.e. a set of three-dimensional points that are contained in the wavefront, which is explained by the discrete measurement of a SHS.

In particular, a spline based approach is used to guarantee an accurate reconstruction [19]. Before registration each measurement is reconstructed, resulting in a set of point clouds, each corresponding to a wavefront segment.

2.2. Registration of two wavefront segments

Ignoring sensor misalignment and taking only the nominal sensor positioning data into account, the point cloud of wavefront segment i in FG is

$$P_{0i} = \{\mathbf{x}_{0i1}, \dots, \mathbf{x}_{0in}\}. \quad (1)$$

Furthermore, let be P_{0i} rigidly transformed and propagated given by the point cloud

$$P_i(\mathbf{a}_i) = B_{\omega_i}(F_{s_i}(P_{0i})) = \{\mathbf{x}_{i1}(\mathbf{a}_i), \dots, \mathbf{x}_{in}(\mathbf{a}_i)\}, \quad (2)$$

where $F_{s_i}(P)$ and $B_{\omega_i}(P)$ denote transformations of a point cloud P in terms of parameters $\mathbf{a}_i = \{s_i, \omega_i\} = \{s_i, \theta_i, \mathbf{k}_i\}$. F_{s_i} in particular denotes the wavefront propagation along a distance $s_i \in \mathbb{R}$ and B_{ω_i} a rigid body transformation with parameters $\mathbf{k}_i, \theta_i \in \mathbb{R}^3$ defining translation and rotation about the center of the respective nominal subaperture (see Fig. 3).

With parameters ω_i^* reflecting the actual misalignment $P_i(0, \omega_i^*)$ constitutes the segment with actual position.

Let FSi be the coordinate system of subaperture i with nominal position, whose x-y plane lies in the plane of the subaperture. Transformation from FSi to FG is given by a rigid body transformation in terms of $\psi_i, \mathbf{v}_i \in \mathbb{R}^3$, denoting the nominal sensor alignment and position. In Fig. 3 the defined coordinate systems and point clouds are illustrated.

As a requirement for registration a metric has to be defined for the mismatch between wavefronts. For this, point clouds $P_1(\mathbf{a}_1)$ and $P_2(\mathbf{a}_2)$ of overlapping wavefront segments 1 and

M_{12} still can be used for registration of $P_1(\mathbf{a}_1)$ and $P_2(\mathbf{a}_2)$. This is because M_{12} gets minimized for the same parameters as \tilde{M}_{12} , i.e. if and only if

$$\tilde{M}_{12}(A_{12}^*) = \min\{\tilde{M}_{12}\} \quad \text{then} \quad (7a)$$

$$M_{12}(A_{12}^*) = \min\{M_{12}\} \quad (7b)$$

Proof

1. As two matching wavefronts still match if both are propagated equally by $\eta \in \mathbb{R}$, it is inferred that

$$\min\{\tilde{M}_{12}\} = \tilde{M}_{12}(s_1^* + \eta, \omega_1^*, s_2^* + \eta, \omega_2^*). \quad (8)$$

Setting $\eta = -s_1^*$ leads to

$$\min\{\tilde{M}_{12}\} = \tilde{M}_{12}(0, \omega_1^*, s_2^* - s_1^*, \omega_2^*) = M_{12}(A_{12}^*). \quad (9)$$

2. Two wavefronts that do not match can not be registered by any uniform propagation $\eta \in \mathbb{R}$. Hence, if $A'_{12} = (s'_1, \omega'_1, s'_2, \omega'_2)$ with $\min\{\tilde{M}_{12}\} < \tilde{M}_{12}(A'_{12})$ then

$$\min\{\tilde{M}_{12}\} < \tilde{M}_{12}(s'_1 + \eta, \omega'_1, s'_2 + \eta, \omega'_2). \quad (10)$$

With $\eta = -s'_1$ and Eq. 9 the following is deduced

$$M_{12}(A_{12}^*) < \tilde{M}_{12}(0, \omega'_1, s'_2 - s'_1, \omega'_2) = M_{12}(A'_{12}). \quad \blacksquare \quad (11)$$

Applying the reverse rigid body transform $B_{\omega_1}^{-1}$ to both point clouds and considering Eq. 2 gives

$$B_{\omega_1}^{-1}(P_1(0, \omega_1)) = P_1(0, 0) = P_{01} \quad (12)$$

and the definition

$$B_{\omega_1}^{-1}(P_{21}(s_2 - s_1, \omega_2)) = \tilde{P}_{21}(s_1, \omega_1, s_2, \omega_2) = \tilde{P}_{21}(A_{12}). \quad (13)$$

With Eq. 5, 12 and 13 and the fact that $\Delta(\cdot, \cdot)$ is invariant under rigid body transformations of the point clouds the following equation can be written

$$M_{12}(A_{12}) = \Delta(P_{01}, \tilde{P}_{21}(A_{12})). \quad (14)$$

Registration with Eq. 14 instead of Eq. 4 provides two advantages. First, one point cloud, i.e. P_{01} is independent of the parameters, providing the benefit that a reduced number of points need to be transformed, which decreases computation time. Second, interpolation of P_{01} has to be carried out only once and not after every change of A , which also decreases computation time. To outline these advantages, the considered point clouds and their dependence on parameters are illustrated in Fig. 4.

Although, M_{12} is invariant under the coordinate system in which the point clouds are represented, it is proposed to compute the metric in FS1, i.e.

$$M_{12}(A_{12}) = \Delta(P_{01}^1, \tilde{P}_{21}^1(A_{12})), \quad (15)$$

where the upper index refers to the coordinate system in which an object is represented. One reason for this is that with reconstruction of a wavefront segment i P_{0i}^i is determined. Hence, P_{01}^1 is right after wavefront reconstruction available and no additional transformation of the

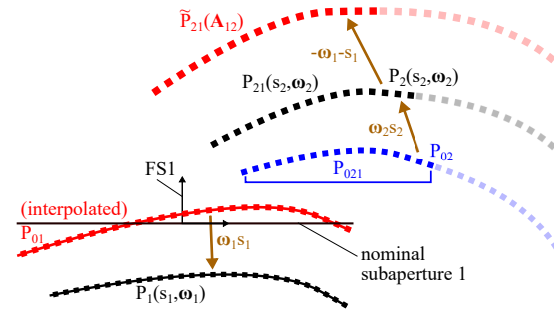


Fig. 4. Point clouds of wavefront segment 1 and 2 with dependence on parameters $A_{12} = (s_1, \omega_1, s_2, \omega_2)$. In Eq. 4 $P_1(s_1, \omega_1)$ and $P_{21}(s_2, \omega_2)$ are used for registration and in Eq. 14 P_{01} and $\tilde{P}_{21}(A_{12})$. For subpixel registration point clouds of segment 1 are interpolated.

point cloud is necessary. To satisfy Eq. 2 and 13 P_{02}^2 is propagated by $(s_2 - s_1)$ and rigid body transformed by ω_2 and ω_1 leading to

$$\tilde{P}_2^2(A_{12}) = B_{\omega_1}^{-1}(B_{\omega_2}(F_{s_2-s_1}(P_{02}^2))). \quad (16)$$

Transformation from FS2 into FS1 is performed by a rigid body transformation in terms of the nominal positions of the subapertures $\psi_1, \mathbf{v}_1, \psi_2, \mathbf{v}_2$, i.e.

$$\tilde{P}_2^1(A_{12}) = T_{\psi_1, \mathbf{v}_1, \psi_2, \mathbf{v}_2}^{2 \rightarrow 1}(\tilde{P}_2^2(A_{12})). \quad (17)$$

Considering only the points belonging to the overlap with P_{01}^1 $\tilde{P}_{21}^1(A_{12}) \in \tilde{P}_2^1(A_{12})$ is determined. Another advantage of calculating the metric in FS1 is that orthogonal projection of points of \tilde{P}_{21}^1 onto P_{01}^1 can be approximated by a projection along the z-axis. This is explained, due to the limited dynamic range of the SHS, where the maximal measurable tilt of an incoming wavefront is less than 15° [20]. Hence, in FS1 the maximum angle between segment 1 and the x-y plane of the system is smaller than 15° . Moreover, as translational and rotational misalignment of positioning systems is usually at a scale of a few μm and $10 - 100 \mu\text{rad}$, the local change of orientation of a wavefront is much smaller than 15° . Therefore, overlapping wavefront segments can be locally approximated by parallel planes. The stronger these parallel planes are tilted in FS1 the stronger the projection along the z-axis deviates from the orthogonal projection with the phase difference between the segments. However, even in case of maximal tilted planes (15°) and a large phase difference where propagation of $400 \mu\text{m}$ is necessary for compensation, the deviation of the projection along the z-axis from the orthogonal projection is still smaller than $110 \mu\text{m}$. As this is smaller than the typical resolution of a SHS about $130 \mu\text{m}$ [21], the projection along the z-axis is still a good approximation of the orthogonal projection. Projection along the z-axis is quickly determined by evaluation of the interpolant of P_{01}^1 at the x-y coordinates of the point being projected. Therefore, even in case of divergent wavefronts where large sensor angles are necessary and orthogonal projection might be time consuming in FG, it is still quickly determined in FS1 (see Fig. 5).

2.3. Parallel registration of wavefront segments

Eq. 15 provides an efficient way to calculate the overlap mismatch between two wavefronts that are both transformed with the respective rigid body and propagation parameters.

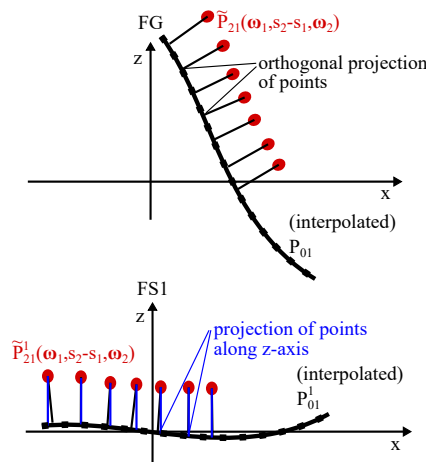


Fig. 5. In FS1 orthogonal projection can be approximated by projection along the z-axis, which is quickly determined by evaluation of the interpolant at the x-y coordinates of the point that is projected.

To get the mismatch of a set of wavefront segments $i = 1..N$, where each is transformed by parameters \mathbf{a}_i the sum over all overlap mismatches between two segments is considered. Hence, a global mismatch metric can be defined using Eq. 15 as the sum over all overlapping wavefront pairs

$$M_g(A) = \sum_{i,k} M_{ik}(A_{ik}) = \sum_{i,k} \Delta(P_{0i}^i, \tilde{P}_{ki}^i(A_{ik})). \quad (18)$$

As mentioned before the first point cloud in $\Delta(\cdot, \cdot)$ gets interpolated. To reduce the amount of interpolations the segments are divided into type1 and type2 segments, which are arranged in a chessboard pattern (see Fig. 6). Each type1 segment is interpolated in the corresponding sub system, while point clouds of type2 segments get reduced to the overlap with the type1 segment based on the corresponding position data.

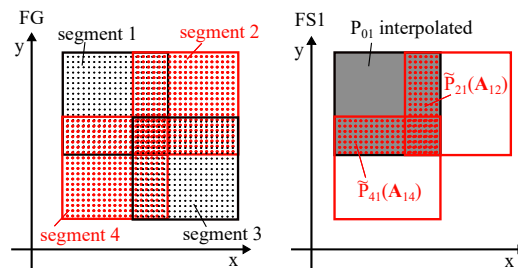


Fig. 6. Primary overlaps are between type1 (black) and type2 (red) segments. A type1 segment gets interpolated in the corresponding sub system, while type2 segments get reduced to the overlapping region.

Minimization of Eq. 18, resembling the parallel registration, is a nonlinear optimization problem. A Quasi-Newton method is chosen for this purpose, as it is an efficient method for

nonlinear optimization [22].

In summary, there are four basic steps of the proposed wavefront reconstruction as illustrated in Fig. 7. First, the zonal reconstruction of the wavefront segments from the measurements is carried out. Second, the interpolation of type1 segments and third, the reduction of type2 segments to the overlap is performed. Fourth, parallel registration of the wavefront segments by minimization of the global mismatch metric is carried out.

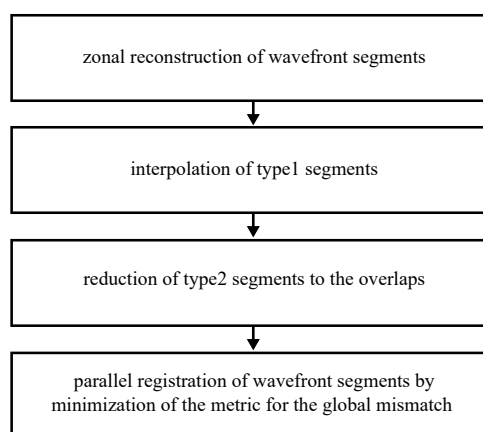


Fig. 7. Basic steps of the parallel registration algorithm.

3. Algorithm analysis

To investigate the properties of the parallel registration (PR) algorithm and examine its dependence on quantities like misalignment, noise, etc., a simulation based analysis is performed.

To evaluate the performance of the PR algorithm, the registered wavefronts are compared to the results of the well established ICP algorithm [23].

3.1. Simulation setting

The wavefront that is registered by the algorithms, is a spherical wavefront collimated by a meniscus lens with a diameter of 50.8 mm and a focal length of 200 mm [24]. The wavefront is determined by using the software OpticStudio (Zemax LLC, Kirkland, WA, USA) and the aberration has a peak to valley of $11\text{ }\mu\text{m}$ with a dominating spherical aberration (see Fig. 8). The size of the wavefront with a diameter of about 50 mm exceeds the sensor aperture of a standard SHS by a factor about 3 [21]. Furthermore, shrinking the wavefront would need additional optical systems that cause additional aberrations and corrupt the measurement. The wavefront is virtually measured using 5×5 subapertures with a self developed tool based on MATLAB (The MathWorks Inc., Natick, MA, USA), as illustrated in Fig. 8. Each subaperture constitutes a square with a side length of 13 mm and all subapertures are located in the x-y plane. The number of lenslets, i.e. the number of spots per subaperture where the gradient of the wavefront is measured, is set to a standard sensor configuration comprising 100×100 lenslets, each with a size of $130 \times 130\text{ }\mu\text{m}^2$ [21]. To mimic a realistic measurement, errors like sensor misalignment as well as measurement noise are simulated. The algorithms are then used to reconstruct the wavefront from the set of simulated measurements. For subpixel accuracy cubic interpolation is used to interpolate the point clouds of type1 segments. Cubic interpolation is preferred as by comparison with the nominal shape of the wavefront the peak to valley interpolation error is

about 2 nm for linear interpolation and 0.01 nm for cubic interpolation.

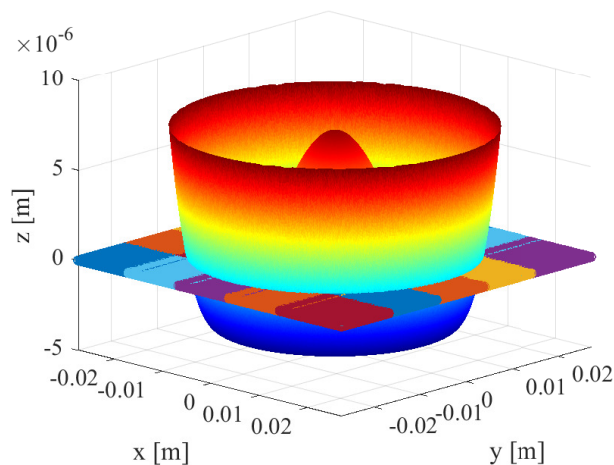


Fig. 8. Wavefront for algorithm evaluation ($PV = 11\text{ }\mu\text{m}$). The wavefront is generated by propagation of a spherical wavefront through a meniscus lens. The wavefront is virtually measured over a 5×5 subaperture matrix in the x-y plane. At each subaperture a measurement with the SHS is simulated with 100×100 lenslets.

For initialization of the ICP algorithm a segment is set as the partially registered wavefront. Then individual registration processes are carried out sequentially, where in each process the partially registered wavefront is extended by a wavefront segment stitched onto it. The segments are registered in a spiral way (see Fig. 9).

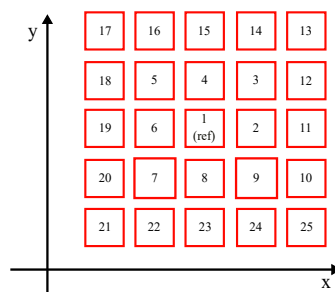


Fig. 9. Wavefront segments are sequentially stitched in a spiral way using ICP algorithm. The initial subaperture is in the center.

For the evaluation of an algorithm result, the deviation of the registered wavefront from the exact wavefront is determined. In particular, the registered wavefront is fitted into the exact one and the difference between the wavefronts is computed. The noise distribution added before the reconstruction process for augmenting measurement uncertainties is removed from the difference to get the error distribution only due to registration errors. For comparison the root mean square

(RMS) and peak to valley (PV) of the respective wavefront differences are calculated. In Fig. 10 the procedure of testing an algorithm is summarized.

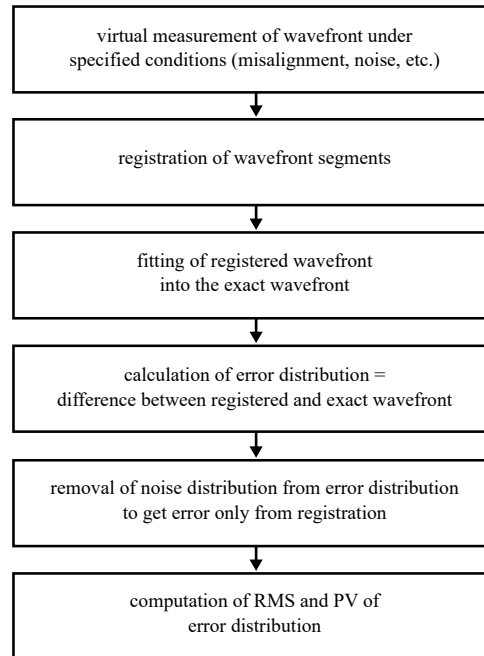


Fig. 10. Steps of simulative testing of the registration algorithms.

3.2. Reference Configuration

As described in Section 2 position and alignment of a subaperture deviate from the nominal position due to sensor misalignment. The misalignment can be described by the rigid body transformation in terms of the six parameters $(\theta_{xi}, \theta_{yi}, \theta_{zi}, k_{xi}, k_{yi}, k_{zi})$, where the first three represent rotational (tilt, tip, azimuthal angle) and the last three translational misalignment. In the simulation each subaperture is misaligned, with the misalignment randomly chosen within predefined ranges for rotational and translational misalignment

$$\begin{aligned} \theta_{xi}, \theta_{yi}, \theta_{zi} &\in [-50, 50] \mu rad, \\ k_{xi}, k_{yi}, k_{zi} &\in [-0.8, 0.8] \mu m. \end{aligned} \quad (19)$$

The values for misalignment ranges are on the order of typical errors of linear and rotational stages [25,26] that can be used for subaperture positioning.

There are several sources of noise in a SHS measurement like background light, readout or dark current [27]. To simulate the impact of these noise sources on the measurement, gaussian noise with zero mean is added to the point cloud of each segment. The reference noise variance is $\sigma = 10 nm$, which is on a typical order for measurement noise [28]

As described in Section 2 only points in the overlap are considered for registration. Using only 100 points per overlap (PPO) for registration might lead to a sufficient reconstruction quality and

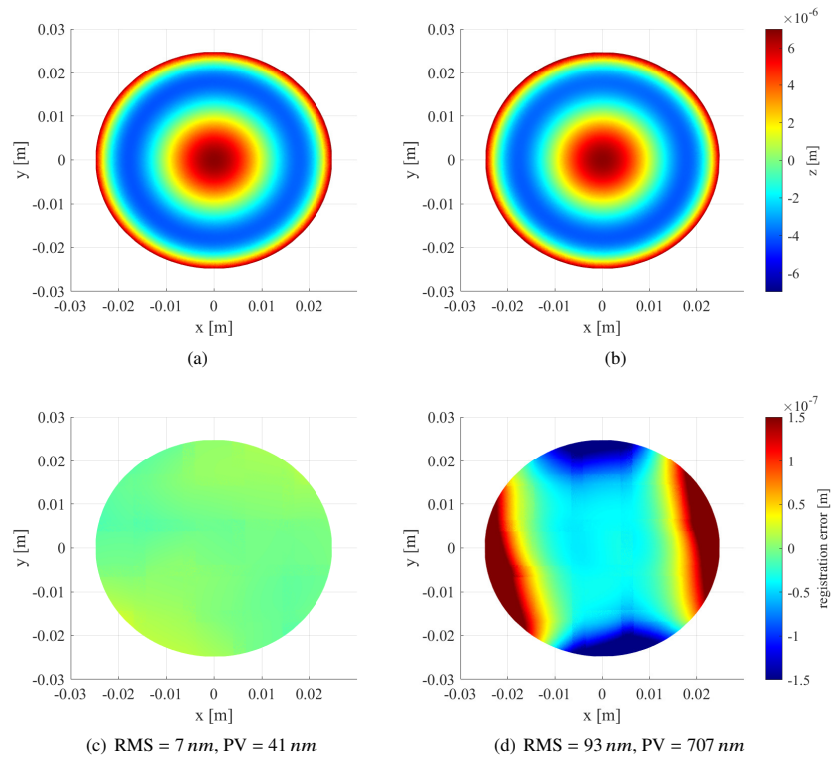


Fig. 11. Registered wavefront (a: PR, b: ICP) and its registration error as compared to the exact wavefront (c: PR, d: ICP) for the reference configuration.

at the same time reduces computation time.

In the following sections both algorithms are analysed with respect to sensor misalignment, measurement noise, number of PPO and the percentage of overlap with respect to the subaperture area that is set to 20 % in reference configuration. Each section focuses on one quantity, which means that based on the aforementioned reference configuration only the quantity under consideration is changed. In Fig. 11 the registered wavefronts of both algorithms are shown together with the corresponding differences to the exact wavefront (see Fig. 8). The differences to the exact wavefront show the superiority of the PR algorithm with an RMS of 7 nm over the ICP algorithm with an RMS of 93 nm. Especially at areas remote from the wavefront center the ICP algorithm shows large errors. This is because registration is carried out in a spiral way, where wavefront segments the more remote they are from the center the later they get registered. As accumulation of registration errors grows with each registration process the outer wavefront segments show larger errors.

3.3. Influence of misalignment

Reconstruction is carried out for different misalignment ranges and the results are shown in Table 1. The results show a clear advantage of the developed parallel registration algorithm with an RMS error value about a factor 10 smaller than the one of the ICP algorithm. This can be

mainly explained by the fact, that with parallel registration the accumulation of stitching errors is reduced.

Due to measurement noise, the mismatch metric changes and the global minimum gets shifted as well as local minima emerge causing registration errors. The small errors of the PR algorithm ($\approx 8 \text{ nm}$) show the robustness of the global mismatch metric (see Eq. 18) to the measurement noise. The results show that the considered misalignment ranges do not strongly affect the registration performance. Both algorithms show a rather constant RMS error for the various parameter sets. Only for large translational misalignment around $10 \mu\text{m}$ the errors slightly increase. Although, there is some uncertainty between the results, it does not correlate with misalignment ranges. A reason for the small variations of the results might be local minima in the mismatch metric caused by the noise. With a different initial position the algorithm converges differently to the global minimum of the mismatch metric and gets caught in different local minima around the global minimum.

Table 1. **Error of registered wavefront of parallel registration (PR) and iterative closest point (ICP) for different rotational and translational misalignment ranges $\pm r_\theta$ and $\pm r_k$.**

r_θ	r_k	PR	PR	ICP	ICP
(μrad)	(μm)	RMS (nm)	PV (nm)	RMS (nm)	PV (nm)
15	0,5	7	36	91	734
50	0,5	7	42	95	813
100	0,5	7	39	82	654
200	0,5	6	39	94	743
300	0,5	8	50	82	670
15	1	6	37	88	660
15	2	6	36	83	614
15	5	8	53	94	752
15	10	11	76	94	732
50	0,8	7	41	93	707
75	1	6	38	96	795
100	2	7	41	91	710
200	5	7	48	98	714
300	10	12	79	93	696

3.4. Influence of noise

Variances of measurement noise between 2 nm and 30 nm are considered. Fig. 12 shows the RMS error of the results of both algorithms. Additionally, for the PR algorithm the RMS error without noise removal is plotted to illustrate the direct contribution of noise to the difference.

For both algorithms the RMS error increases rather linearly with the noise variance. While the RMS error of the PR algorithm increases by only 16 nm for the considered σ -range, the RMS error of the ICP algorithm is much more sensitive to noise and increases by 166 nm . The

robustness of the PR algorithm to noise is explained by the reduced accumulation of stitching errors compared to the ICP algorithm. For all noise variances errors of the PR algorithm are about a factor 10 smaller than the errors of the ICP algorithm. Typically, wavefronts of as-built optical systems contain RMS errors at a scale of 500 nm [29] down to a scale of a few nanometers [30]. In case of a low measurement noise ($\sigma < 2 \text{ nm}$) the PR algorithm has a RMS error smaller 3 nm making the algorithm suitable for the evaluation of high-end optical systems with RMS wavefront errors about 10 nm.

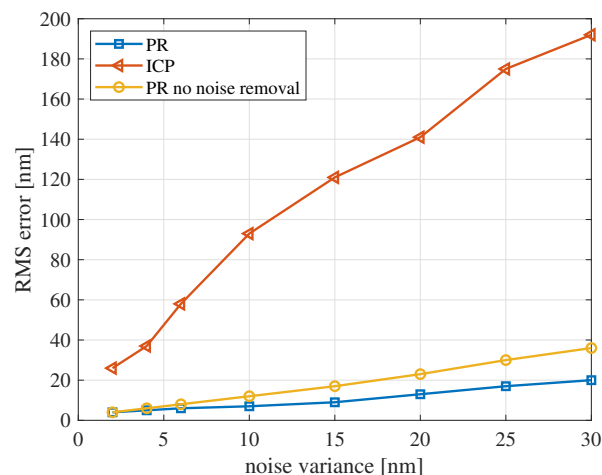


Fig. 12. Error of registered wavefront (RMS) of PR algorithm with and without noise removal and ICP algorithm in terms of noise variance.

3.5. Influence of points per overlap

In Fig. 13 the RMS registration error in terms of the number of PPO is plotted for both algorithms. A number of PPO from 50 to 500 is considered.

The errors of both algorithms decrease with a larger number of PPO, which is explained by two reasons. First, the impact of noise is reduced due to taking the average of a larger number of points. Second, with a larger number of PPO more information of the surface shape is available and hence registration is more accurate.

While the RMS error of the PR algorithm depends linearly on the number of PPO the RMS error of the ICP algorithm shows nonlinearities and is quite sensitive for a number of PPO smaller 100. For a number of PPO above 100 the PR errors are about a factor 10 smaller than the errors of the ICP algorithm. For a low number of PPO of 50 the ICP algorithm errors strongly increase to a RMS of 175 nm, while the PR algorithm still has a small RMS error of 8 nm. This proves the reliability of the PR algorithm in cases where a low amount of surface information is available.

3.6. Influence of overlap size

To increase the overlap the subapertures are enlarged. The size of the lenslets remains constant to maintain the sensor resolution. Overlaps of 20 %, 30 % and 40 % of the subaperture area are considered with subaperture side lengths of 13 mm, 14.82 mm and 17.16 mm respectively. The results are shown in Table 2. The errors of both algorithms decrease with a larger overlap area. One reason for this is that with a larger overlap the mismatch metric gets more sensitive to angles

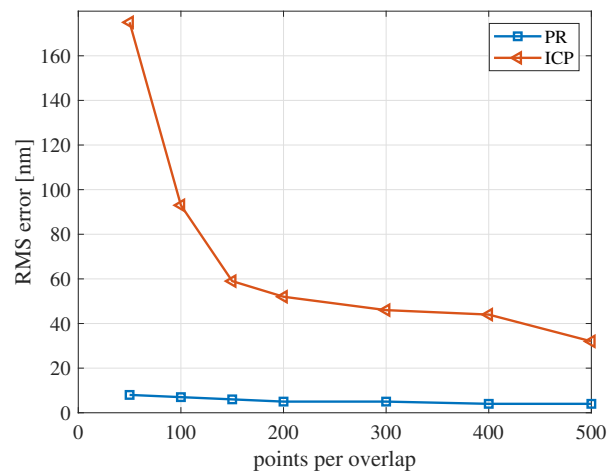


Fig. 13. Error of registered wavefront (RMS) of PR algorithm and ICP algorithm in terms of the number of points per overlap.

between the wavefront segments. Another reason is that on a larger area larger variations of the wavefronts shape are observed increasing the signal-to-noise ratio. An increase of overlap percentage from 20 % to 40 % results in a decrease of the errors of the PR algorithm by 55 % and of the ICP algorithm by 70 %, but would require a larger amount of measurements per subaperture and thus increases measurement time. With an overlap percentage of 40 % the PR algorithm has an RMS error of 3 nm. Hence, despite a noise variance of 10 nm the PR algorithm reaches a registration accuracy that enables the evaluation of high-end optical systems with RMS wavefront errors about 10 nm.

Table 2. Results for different overlap sizes. Error of registered wavefront of parallel registration (PR) and iterative closest point (ICP) is listed.

overlap (%)	PR RMS (nm)	PR PV (nm)	ICP RMS (nm)	ICP PV (nm)
20	7	41	93	707
30	4	26	49	382
40	3	20	28	200

In summary the functionality of the developed parallel registration algorithm is successfully demonstrated, showing its high resilience to sensor misalignment and measurement noise and superior performance as compared to the ICP algorithm. The registration errors of the PR algorithm are about a factor 10 smaller than the registration errors of the ICP algorithm. Moreover, despite measurement noise the PR algorithm reaches registration accuracies suitable for the evaluation of high-end optical systems with RMS wavefront errors about 10 nm.

4. Conclusions

In this paper, an algorithm for wavefront reconstruction from multiple SHS measurements is proposed. In particular, the reconstruction is carried out by parallel registration of the measured wavefront segments. Mathematics of the algorithm are discussed and wavefront reconstruction despite rigid body sensor misalignment or phase difference between the measurements is possible. The performance of the parallel registration algorithm is simulatively analysed and compared with sequential registration based on the established ICP algorithm. The analysis is carried out with respect to sensor misalignment, measurement noise, number of points per overlap and the percentage of overlap with respect to the subaperture area. While the ICP algorithm is quite sensitive to measurement noise and low surface information the parallel registration algorithm is more robust and has registration errors about a factor 10 smaller than those of the ICP algorithm. Results show that even in challenging cases with, e.g. large measurement noise, the parallel registration algorithm achieves qualitative wavefront reconstruction with a RMS registration error of 10 nm to 20 nm, while the RMS registration error of the ICP is 100 nm to 200 nm. The superiority of the parallel registration algorithm is mainly explained by the reduced accumulation of registration errors. This is due to the fact that in parallel registration for minimization of the mismatch in an overlap between two wavefront segments the surface information of all overlaps is used. Hence, the parallel registration algorithm better exploits the surface information of overlaps than the ICP algorithm. Considering a wavefront of a meniscus lens the PR algorithm reaches RMS registration errors smaller 3 nm making the evaluation of high-end optical systems with 10 nm RMS wavefront errors possible.

5. Funding.

Austrian Federal Ministry for Digital and Economic Affairs; National Foundation for Research, Technology and Development; MICRO-EPSILON MESSTECHNIK GmbH & Co. KG; ATENSOR Engineering and Technology Systems GmbH.

6. Acknowledgement.

We thank Johannes Pfund and Ralf Dorn from Optocraft GmbH for their support and fruitful discussions. The financial support by the Christian Doppler Research Association, the Austrian Federal Ministry for Digital and Economic Affairs, and the National Foundation for Research, Technology and Development, as well as MICRO-EPSILON MESSTECHNIK GmbH & Co. KG and ATENSOR Engineering and Technology Systems GmbH is gratefully acknowledged.

7. Disclosures.

The authors declare no conflicts of interest.

References

1. J. Sheldakova, A. Kudryashov, V. Zavalova, and P. Romanov, "Shack-hartmann wavefront sensor versus fizeau interferometer for laser beam measurements," in *Laser Resonators and Beam Control XI*, vol. 7194 (International Society for Optics and Photonics, 2009), p. 71940B.
2. J. Pfund, M. Beyerlein, and R. Dorn, "Shack-hartmann sensors for industrial quality assurance," in *Adaptive Optics for Industry and Medicine*, (Springer, 2005), pp. 141–150.
3. J. Liang, B. Grimm, S. Goelz, and J. F. Bille, "Objective measurement of wave aberrations of the human eye with the use of a hartmann-shack wave-front sensor," *JOSA A* **11**, 1949–1957 (1994).
4. C. Véraud, M. Le Louarn, V. Korkiakoski, and M. Carbillet, "Adaptive optics for high-contrast imaging: pyramid sensor versus spatially filtered shack–hartmann sensor," *Mon. Notices Royal Astron. Soc. Lett.* **357**, L26–L30 (2005).
5. M. Thier, R. Paris, T. Thurner, and G. Schitter, "Low-latency shack–hartmann wavefront sensor based on an industrial smart camera," *IEEE Transactions on Instrumentation Meas.* **62**, 1241–1249 (2012).
6. D. R. Neal and J. Mansell, "Application of shack-hartmann wavefront sensors to optical system calibration and alignment," in *Adaptive Optics For Industry And Medicine*, (World Scientific, 2000), pp. 234–240.

7. M. Rocktäschel and H. Tiziani, "Limitations of the shack-hartmann sensor for testing optical aspherics," *Opt. & Laser Technol.* **34**, 631–637 (2002).
8. M. Fuerst, S. Unger, S. Ito, and G. Schitter, "Wavefront measurement based feedback control for automatic alignment of a high-na optical system," in *Journal of Physics: Conference Series*, vol. 1065 (2018).
9. M. E. Fuerst, E. Csencsics, N. Berlakovich, and G. Schitter, "Automated measurement of highly divergent optical wavefronts with a scanning shack-hartmann sensor," *IEEE Transactions on Instrumentation Meas.* (2020).
10. M. E. Fuerst and G. Schitter, "Scanning wavefront sensor for measurement of highly divergent wavefronts," *IFAC-PapersOnLine* **52**, 25–30 (2019).
11. D. R. Burada, K. K. Pant, M. Bichra, G. S. Khan, S. Sinzinger, and C. Shakher, "Experimental investigations on characterization of freeform wavefront using shack-hartmann sensor," *Opt. Eng.* **56**, 084107 (2017).
12. K. K. Pant, D. R. Burada, M. Bichra, M. P. Singh, A. Ghosh, G. S. Khan, S. Sinzinger, and C. Shakher, "Subaperture stitching for measurement of freeform wavefront," *Appl. optics* **54**, 10022–10028 (2015).
13. K. K. Pant, D. R. Burada, M. Bichra, A. Ghosh, G. S. Khan, S. Sinzinger, and C. Shakher, "Weighted spline based integration for reconstruction of freeform wavefront," *Appl. optics* **57**, 1100–1109 (2018).
14. K. K. Pant, D. R. Burada, A. Ghosh, G. S. Khan, and C. Shakher, "Improved subaperture stitching for the measurement of freeform wavefront," in *Laser Science*, (Optical Society of America, 2018), pp. JW4A–9.
15. R. Bergevin, M. Soucy, H. Gagnon, and D. Laurendeau, "Towards a general multi-view registration technique," *IEEE Transactions on Pattern Analysis Mach. Intell.* **18**, 540–547 (1996).
16. I. Mochi and K. A. Goldberg, "Modal wavefront reconstruction from its gradient," *Appl. Opt.* **54**, 3780–3785 (2015).
17. W. H. Southwell, "Wave-front estimation from wave-front slope measurements," *JOSA* **70**, 998–1006 (1980).
18. L. Huang, J. Xue, B. Gao, C. Zuo, and M. Idir, "Zonal wavefront reconstruction in quadrilateral geometry for phase measuring deflectometry," *Appl. optics* **56**, 5139–5144 (2017).
19. L. Huang, J. Xue, B. Gao, C. Zuo, and M. Idir, "Spline based least squares integration for two-dimensional shape or wavefront reconstruction," *Opt. Lasers Eng.* **91**, 221–226 (2017).
20. Optocraft GmbH, *SHSLab (Produktbroschüre)* (2019).
21. Optocraft GmbH, *SHSCam standard sensor head overview* (2019).
22. P. E. Gill, W. Murray, and M. H. Wright, *Practical optimization* (SIAM, 2019).
23. P. J. Besl and N. D. McKay, "Method for registration of 3-d shapes," in *Sensor fusion IV: control paradigms and data structures*, vol. 1611 (International Society for Optics and Photonics, 1992), pp. 586–606.
24. Thorlabs inc., *N-BK7 Positive Meniscus Lens, LE1015-A* (2009).
25. Physik Instrumente (PI) GmbH & Co. KG, *PRS-200 Präzisions-Rotationstisch, 6449921111* (2020).
26. Physik Instrumente (PI) GmbH & Co. KG, *V-551 Präzisions-Lineartisch, V-551.2x* (2020).
27. H. Mao, Y. Liang, J. Liu, and Z. Huang, "A noise error estimation method for shack-hartmann wavefront sensor," in *AOPC 2015: Telescope and Space Optical Instrumentation*, vol. 9678 (International Society for Optics and Photonics, 2015), p. 967811.
28. C. Li, H. Xian, W. Jiang, and C. Rao, "Wavefront error caused by centroid position random error," *J. Mod. Opt.* **55**, 127–133 (2008).
29. K. Fuerschbach, G. E. Davis, K. P. Thompson, and J. P. Rolland, "Assembly of a freeform off-axis optical system employing three φ -polynomial zernike mirrors," *Opt. Lett.* **39**, 2896–2899 (2014).
30. D. S. Anderson, J. R. P. Angel, J. H. Burge, W. B. Davison, S. T. DeRigne, B. Hille, D. A. Ketelsen, W. C. Kittrell, H. M. Martin, R. H. Nagel *et al.*, "Stressed-lap polishing of 3.5-mf/1.5 and 1.8-mf/1.0 mirrors," in *Advanced optical manufacturing and testing II*, vol. 1531 (International Society for Optics and Photonics, 1992), pp. 260–269.